

Effects of Li additions on precipitation-strengthened Al–Sc and Al–Sc–Yb alloys

M.E. Krug^a, D.C. Dunand^a, D.N. Seidman^{a,b,*}

^a Department of Materials Science and Engineering, Northwestern University, 2220 Campus Drive, Evanston, IL 60208, USA

^b Northwestern University Center for Atom-Probe Tomography (NUCAPT), 2220 Campus Drive, Evanston, IL 60208, USA

Received 15 October 2010; received in revised form 11 November 2010; accepted 15 November 2010

Available online 17 December 2010

Abstract

Two Al–Sc-based alloys (Al–0.12Sc and Al–0.042Sc–0.009Yb, at.%) and their counterparts with Li additions (Al–2.9Li–0.11Sc and Al–5.53Li–0.048Sc–0.009Yb, at.%) are aged at 325 °C. For both base alloys, the addition of Li results in greater peak hardness from incorporation of Li in the L1₂-structured α' -Al₃(Sc,Li) and α' -Al₃(Sc,Li,Yb) precipitates, and a concomitant increase in number density and volume fraction of the precipitates and a reduction in their mean radius. These changes result from a combination of: (i) an increase in the driving force for precipitate nucleation due to Li; (ii) a decrease in the elastic energy of the coherent misfitting precipitates from a decrease in their lattice parameter mismatch due to their Li content; and (iii) a decrease in the interfacial free energy, as determined from measurements of the relative Gibbsian interfacial excess of Li. In Al–2.9Li–0.11Sc (at.%), the Li concentration of the precipitates decreases from 9.1 at.% in the peak-aged state (8 h) to 5.7 at.% in the over-aged state (1536 h). As a result, the precipitate volume fraction decreases from 0.56% at peak aging time to 0.45% at 1536 h. In Al–5.53Li–0.048Sc–0.009Yb (at.%), the relatively limited Li concentration produces only a small increase in Vickers microhardness from precipitation of metastable δ' -Al₃Li upon a second aging at 170 °C following the primary aging at 325 °C.

© 2010 Acta Materialia Inc. Published by Elsevier Ltd. All rights reserved.

Keywords: Aluminum alloys; Atom-probe field-ion microscopy; Rare earth; Nanostructure; Precipitation

1. Introduction

Aluminum alloys containing dilute additions of Sc and rare-earth (RE) elements are of interest for structural applications, where high-strength at ambient and elevated temperature is important [1,2]. On a per-atom basis Sc offers the greatest improvement of all strengthening alloying additions to Al [3], owing to the precipitation of a high number density of spheroidal nanometer-diameter L1₂-structured Al₃Sc precipitates, which are coherent with the α -Al matrix [2,4–8].

Additions of RE elements reduce the cost of binary Al–Sc-based alloys [9] by replacing more-expensive Sc on

its sublattice in Al₃Sc [10–14] and thereby improving the creep resistance [14,15], without compromising the ambient-temperature strength of the age-hardened alloys [16,17]. Additions of transition elements Ti and Zr, which also substitute for Sc, have also been made to Al–Sc alloys, improving their coarsening resistance [18–24]. While Zr segregates strongly at the α -Al matrix/precipitate interface [20,22], RE elements partition to the precipitate cores, yielding a RE-rich core and a Sc-rich shell [16,17]. Additions of Mg [25–31] and Li [32–37] have also been made to binary Al–Sc alloys. While both Li and Mg additions provide solid-solution strengthening, only Li partitions significantly to the precipitate phase formed during aging at temperatures near 300 °C, resulting in α' -Al₃(Sc,Li) precipitates [36–38].

Two quaternary Al–Li–Sc–X alloys were also investigated previously: Al–6.30Li–0.36Sc–0.13Zr [39] and Al–6.3Li–0.07Sc–0.02Yb [40,41] (here and in the following,

* Corresponding author at: Department of Materials Science and Engineering, Northwestern University, 2220 Campus Drive, Evanston, IL 60208, USA. Tel.: +1 847 4915370; fax: +1 847 4672269.

E-mail address: seidman@northwestern.edu (D.N. Seidman).

all concentrations are in atomic per cent, unless otherwise indicated). For Al–6.30Li–0.36Sc–0.13Zr [39], a two-step heat treatment was applied: (i) aging at 450 °C produced Sc-rich α' -Al₃(Sc,Li) precipitates with Zr segregated at the precipitate/matrix interface; and (ii) further aging at 190 °C resulted in precipitation of an Al_{0.8}Li_{0.2} shell upon the Sc-rich precipitates, forming a core/shell precipitate. For Al–6.3Li–0.07Sc–0.02Yb [40,41], a two-step heat treatment was also applied: (i) aging at 325 °C produced a first microhardness increase due to core/shell α' -Al₃(Sc,Li,Yb) precipitates with a Yb-rich core and a Sc-rich shell (a high and uniform concentration of Li was present in both core and shell); and (ii) further aging at 170 °C resulted in precipitation of a Li-rich shell (with approximate Al₃Li composition) on some of the Sc- and Yb-rich precipitates, resulting in a second population of precipitates with a core/double-shell structure, and a further large increase in microhardness [40,41]. Owing to Li-incorporation in the α' -Al₃(Sc,Li,Yb) precipitates formed at 325 °C, the precipitate volume fraction was increased to 0.33%, from 0.25% achievable in the same alloy without Li. Also, for isothermal aging at 325 °C a plateau in the peak microhardness was measured, which resisted over-aging to 336 h [40,41], while a similar Li-free alloy began to over-age after only 100 h of isothermal aging at 300 °C [16]. Li additions, therefore, promote resistance to over-aging.

The present work builds on previous findings [40,41] by investigating quantitatively the effect of Li additions on an Al–Sc and an Al–Sc–Yb alloy: first, how a Li addition affects the strengthening behavior and resistance to over-aging of isothermally aged Al–Sc(–Yb) alloys; second, the effect of a Li-addition on the physical characteristics (number density, average radius and volume fraction) and chemical compositions of α' -Al₃(Sc,Li,(Yb)) precipitates in peak-aged Al–Li–Sc(–Yb); third, the time evolution of α' -Al₃(Sc,Li) precipitates during isothermal aging of Al–Li–Sc; and, finally, the issue of how to optimize the strength of an Al–Li–Sc–Yb alloy for ambient-temperature strength through double-aging [40,41], while also maintaining creep and coarsening resistance at elevated-temperatures. This entails reducing the solute concentrations from those in Ref. [40,41], to avoid grain-refining primary precipitates, while still retaining a significant strengthening effect due to both α' -Al₃(Sc,Li,Yb) and metastable δ' -Al₃Li precipitates.

2. Experimental

Two Al–Sc-based alloys with measured compositions of Al–0.12Sc and Al–0.042Sc–0.0088Yb (at.%) and their counterparts with Li additions (measured compositions: Al–2.9Li–0.11Sc and Al–5.53Li–0.048Sc–0.0092Yb, at.%) were studied; they are hereafter denoted by Al–Sc and Al–Sc–Yb, and Al–Li–Sc and Al–Li–Sc–Yb, respectively. All four alloys contained silicon at levels typical of commercially cast alloys (0.01–0.02 at.%). The two Li-containing alloys were cast by heating 99.999% pure Al to 800 °C in an induction furnace under an Ar-overpressure of 3 atm.

Small pieces of Al–0.82 at.% Sc and Al–3.7 at.% Yb master alloys prepared by arc-melting of pure elements, and 99.9% pure Li were added to the melt, which was stirred inductively. The melt was then cast into a SiC crucible, resulting in a billet ~4.5 cm in diameter and ~17 cm long. For these Li-containing alloys, the SiC crucible material introduced a measurable concentration of Si into the melt (Table 1). The two Li-free alloys were cast by heating 99.999% pure Al to 750 °C in a zirconia-coated alumina crucible, placed in a resistively heated furnace in an atmosphere of air. Pieces from the same Al–Sc and Al–Yb master alloys and from an Al–12.3 at.% Si master alloy (prepared by arc-melting) were added to the melt. In the Li-free alloys, Si was intentionally added to the melt to ensure that its concentration was similar to their Li-containing counterparts. The melt was stirred mechanically before casting into a graphite mold, which was placed on an ice-chilled copper platen to encourage directional solidification. The casting consisted of four cylinders, ~1 cm in diameter and 10 cm long. Chemical compositions of arc-melted master alloys and homogenized final alloys were measured by direct-current plasma mass-spectroscopy (DCP-MS) by ATI Wah Chang. In some cases, the compositions of the homogenized final alloys were verified by Exova using DCP-MS.

The cast alloy billets were homogenized at 640 °C for 24 h under an atmosphere of air or flowing Ar (for the Li-free and Li-containing alloys, respectively), and quenched into ambient temperature water. The billets were then cut into ~10 × 10 × 4 mm³ specimens, which were homogenized for 20 min as described above, and then quenched into iced brine at a temperature of –12 °C. These specimens were either aged immediately or stored in liquid nitrogen to avoid ambient-temperature aging.

The two Li-bearing alloys were aged isochronally to determine an appropriate aging temperature for isothermal aging studies. The specimens were placed in a furnace in a flowing Ar atmosphere, and the temperature was increased hourly in increments of 25 °C, from 100 to 450 °C. For example, a specimen whose last isochronal aging temperature was at 125 °C was homogenized, quenched, aged at 100 °C for 1 h, aged for 125 °C for 1 h, then quenched in to iced brine at –12 °C. Subsequently, isothermal aging heat treatments were performed on another series of homogenized specimens, which were aged in flowing Ar at 325 °C, for time increments between 10 s and 64 days. Aging treatments of 20 min and shorter were performed in a molten saltbath (NaNO₂–NaNO₃–KNO₃). For both isochronal and isothermal treatments, the aged specimens were mounted in cold-curing epoxy (maximum curing temperature 27 °C) before being ground and polished to a 1 μm surface finish. At least 1 mm was ground from the surface at which hardness was measured, to remove the Li-depleted surface layer produced during heat treatment. Vickers microhardness (HV) measurements were performed at ambient temperature using a 200 g load applied for 5 s. At least 10 indentations per specimen were made including several grains, and all measurements are reported with two

Table 1
Composition of four Al(-Li)-Sc (-Yb) alloys, as determined by DCP-MS and by LEAP tomographic spectrometry.^a

| Alloy | Technique | Li (at.%) | Sc (at.ppm) | Si (at.ppm) | Yb (at.ppm) |
|-------------|-----------|---------------|-------------|-------------|-------------|
| Al-Sc | DCP-MS | – | 1240 ± 30 | 130 ± 10 | – |
| | LEAP | – | 1450 ± 18 | 52 ± 5 | – |
| Al-Li-Sc | DCP-MS | 2.9 ± 0.1 | 1060 ± 73 | 180 ± 11 | – |
| | LEAP | 2.614 ± 0.006 | 1138 ± 13 | 56 ± 4 | – |
| Al-Sc-Yb | DCP-MS | – | 423 ± 5 | 130 ± 3 | 88 ± 1 |
| | LEAP | – | 412 ± 7 | 118 ± 3 | 60 ± 12 |
| Al-Li-Sc-Yb | DCP-MS | 5.53 ± 0.05 | 480 ± 10 | 116 ± 5 | 92 ± 2 |
| | LEAP | 5.612 ± 0.009 | 510 ± 10 | 76 ± 4 | 76 ± 5 |

^a Uncertainty corresponds to two standard deviations from the mean.

standard deviations (SD), such that the reported values are $HV \pm 2SD$. Electrical conductivity was measured at ambient temperature on the same specimens using an eddy-current instrument (Sigmatest 2.069, Foerster Instruments Inc.) at operating frequencies of 120, 240, 480 and 960 kHz.

A Cameca (formerly Imago Scientific Instruments) local-electrode atom-probe (LEAP) 4000X-Si tomograph was employed for studying the alloys at the sub-nanometer scale [42–45]. LEAP tomographic specimens were prepared from the aged specimens by first cutting square parallelepipeds, $0.4 \times 0.4 \times 10 \text{ mm}^3$, which were electropolished at 8–24 VDC, using an electrolyte of 10% perchloric acid in acetic acid, followed by a final electropolish in 2% perchloric acid in butoxyethanol. UV (355 nm) laser light was pulsed at a repetition rate of 500 kHz and at $0.075 \text{ nJ pulse}^{-1}$, to evaporate individual atoms. The specimen temperature was maintained at 35 K, and steady-state DC voltages between 3.5 and 9 kV were applied. Analysis of LEAP data was performed on 3-dimensional (3-D) reconstructions of the specimens using IVAS version 3.4.1 (Cameca). The *z*-dimension (specimen axis) of each reconstructed data set was calibrated by matching interplanar distances in the reconstruction against their literature values at low-index poles. The *x*- and *y*- dimensions (perpendicular to the specimen axis) were calibrated by ensuring that the atomic density of each reconstruction matched the literature value for pure Al. For both calibrations, agreement with the literature values was met to within 5%.

Aged alloys were studied by transmission electron microscopy (TEM), using a Hitachi 8100 microscope at 200 kV. Wafers 150–200 μm thick were cut from aged material using a low-speed diamond saw, and 3-mm-diameter disks were punched from the wafers, which were thinned using a Struers Tenupol 5 electropolisher, with a one part nitric acid to two parts methanol electrolyte. The operating temperature and voltage were $-35 \text{ }^\circ\text{C}$ (dry ice in methanol) and $\sim 20 \text{ VDC}$.

3. Results

3.1. Chemical composition

The chemical compositions of the four alloys, as measured by DCP-MS and by LEAP tomography on homoge-

nized and quenched specimens, are reported in Table 1. Optical and scanning electron microscopy revealed large grains ($\sim 1\text{--}5 \text{ mm}$), and no large primary precipitates were detected. Hence, the solute concentrations measured for the bulk specimens by DCP-MS are expected to be representative of the composition of the matrix as measured by LEAP tomography. There is relatively good agreement between the two measuring techniques, except sometimes in the case of Si and Yb, for which smaller concentrations are measured by LEAP tomography compared with DCP-MS. For Si, this is partly due to an artifact in the spatial detection of Si atoms, which segregate at low-index crystallographic poles (Section 3.4 and Fig. 1). This phenomenon is due to surface migration of the Si solute atoms on the tip during pulsed evaporation, and their preferential retention with respect to Al solute atoms until the atomic terraces evaporate completely. This effect, which is due not to thermally activated diffusion, but rather to species-to-species differences in evaporation fields, has been observed by field-ion microscope imaging of a binary Fe–Si alloy [46]. For Si and Yb, an incorrect detected concentration of solute by LEAP tomography is related to difficulties in making quantitative measurements from the mass spectra for these dilute solutes. For the LEAP tomography operating conditions employed, Si evaporates mainly as $^{28}\text{Si}^{2+}$, whose peak in a mass spectrum can lie in the decay tail of the

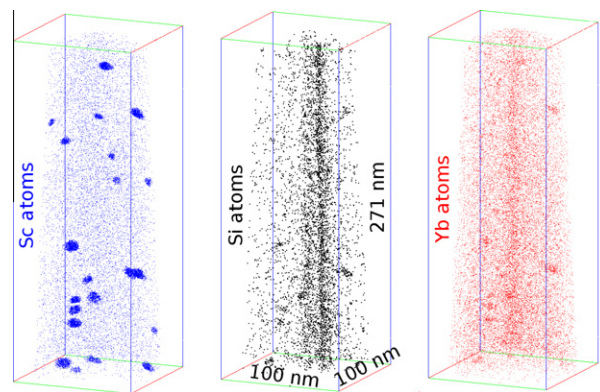


Fig. 1. Three-dimensional LEAP tomographic reconstructions of Al-Sc-Yb aged for 2 h at $325 \text{ }^\circ\text{C}$. Only Sc atoms are shown in the left-most reconstruction, only Si atoms are shown in the center, and only Yb atoms are shown at the right.

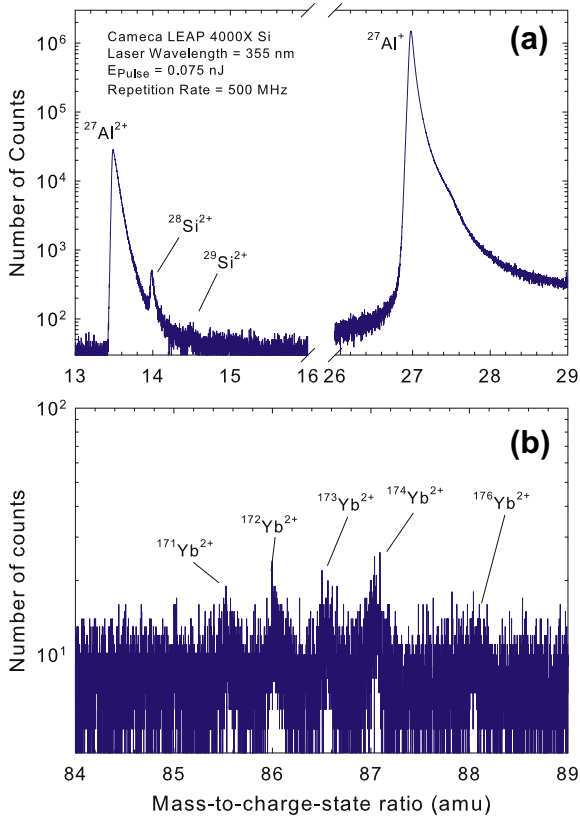


Fig. 2. Mass spectra for (a) Al-Li-Sc aged 8 h at 325 °C and (b) Al-Sc-Yb aged 2 h at 325 °C. In (a) the $^{28}\text{Si}^{2+}$ and $^{29}\text{Si}^{2+}$ peaks lie in the tail of the $^{27}\text{Al}^{2+}$ peak ($^{30}\text{Si}^{2+}$ peak is not resolved). In (b) the main Yb peaks are resolved, but the S/N ratio is low (~ 3 –4).

$^{27}\text{Al}^{2+}$ peak (as illustrated in Fig. 2a for Al-Li-Sc), reducing the accuracy of the concentration measurement. For Yb at ~ 90 at.ppm, quantitative concentration measurements are difficult because four Yb isotopes (171–174) have significant natural abundances. Hence, the signal-to-noise (S/N) ratio for the peaks due to each Yb isotope is small, at ~ 3 –4 (Fig. 2b).

3.2. Isochronal aging

The Vickers microhardness values are displayed in Fig. 3a as a function of the last aging temperature for the two Li-bearing alloys. At final aging temperatures < 200 °C, microhardness for both alloys is unchanged from the unaged value, indicating an incubation stage. The average microhardness value of Al-Li-Sc in this incubation stage is 270 ± 16 MPa, while for Al-Li-Sc-Yb it is 338 ± 56 MPa, as expected from solid-solution strengthening by Li (homogenized Al-Sc-RE alloys without Li additions typically exhibit microhardness values of ~ 220 MPa). Al-Li-Sc reaches a peak microhardness value of 780 ± 30 MPa at a final aging temperature of 325 °C, whereas Al-Li-Sc-Yb reaches a peak microhardness value of 670 ± 50 MPa at a final aging temperature of 350 °C. For higher final aging temperatures the microhardness values of both alloys decrease, but even at the highest mea-

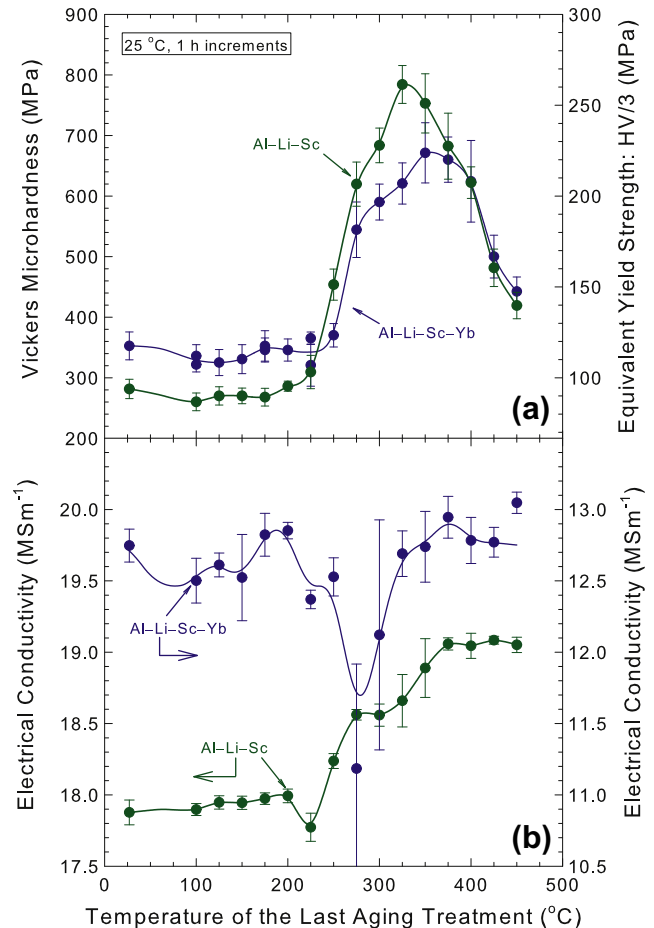


Fig. 3. (a) Vickers microhardness vs. final aging temperature for isochronally aged Al-Li-Sc and Al-Li-Sc-Yb. Aging temperatures are in increments of 25 °C for a dwell time of 1 h. Error bars correspond to 2SD (i.e., error range is 4SD).

sured temperature of 450 °C, they remain higher than the as-homogenized and quenched values. Because the maxima in microhardness occur at 325 and 350 °C for Al-Li-Sc and for Al-Li-Sc-Yb, respectively, the former temperature was chosen for isothermal aging studies of all alloys, to obtain the maximum precipitation hardening effect at a reasonable timescale, while avoiding rapid coarsening or dissolution of α' -Al₃(Sc,Li,Yb) precipitates responsible for the drop in microhardness. The electrical conductivities of the two Li-bearing alloys are displayed in Fig. 3b. For temperatures up to 200 °C, the conductivities of Al-Li-Sc and Al-Li-Sc-Yb remain unchanged from the as-homogenized and quenched values. The initial conductivity values of Al-Li-Sc are greater than those of Al-Li-Sc-Yb, due to the larger concentration of Li in solid solution in the latter alloy. A decrease in conductivity occurs at 225 °C for Al-Li-Sc and at 275 °C for Al-Li-Sc-Yb. For both alloys, this corresponds to the first temperature at which the microhardness increases above the measurement uncertainty from the as-quenched value, indicating that it is related to the onset of a nucleation or precipitation event. The conductivity of Al-Li-Sc increases from 17.9 ± 0.1 MS m⁻¹ to

$19.06 \pm 0.03 \text{ MS m}^{-1}$ during the aging treatment, achieving its upper plateau value at $375 \text{ }^\circ\text{C}$. By contrast for Al–Li–Sc–Yb, excepting the sharp decrease centered at $275 \text{ }^\circ\text{C}$, the conductivities change little during isochronal aging: from $12.6 \pm 0.4 \text{ MS m}^{-1}$ for $T \leq 250 \text{ }^\circ\text{C}$ and to $12.8 \pm 0.4 \text{ MS m}^{-1}$ for $T \geq 325 \text{ }^\circ\text{C}$.

3.3. Isothermal aging

The Vickers microhardness is displayed in Fig. 4a as a function of aging time at $325 \text{ }^\circ\text{C}$ for Al–Sc and the corresponding Al–Li–Sc alloy. Both alloys exhibit an incubation period during which no change in microhardness occurs, lasting up to 2 min for Al–Li–Sc, and up to 10 min for Al–Sc. The plateau's maximum microhardness has a smaller value and duration in Al–Sc ($704 \pm 51 \text{ MPa}$, 1–24 h) compared with Al–Li–Sc ($806 \pm 49 \text{ MPa}$, 20 min–96 h).

The conductivities of Al–Sc and Al–Li–Sc are plotted in Fig. 4b as a function of aging time at $325 \text{ }^\circ\text{C}$. Similar to the microhardness evolution, both alloys exhibit an initial incubation period, lasting up to 5 min for Al–Sc and up to 2 min for Al–Li–Sc. Thereafter, both alloys exhibit a rapid increase in conductivity followed by a slower

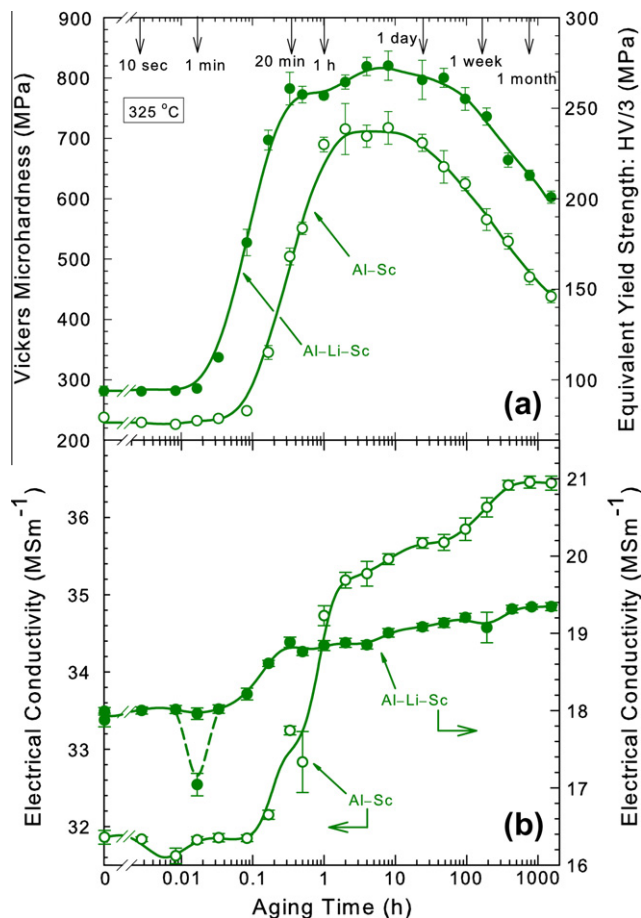


Fig. 4. (a) Vickers microhardness vs. aging time and (b) electrical conductivity vs. aging time for Al–Sc and Al–Li–Sc aged isothermally at $325 \text{ }^\circ\text{C}$. Error bars correspond to 2SD (i.e., error range is 4SD).

increase, and finally a plateau for aging times of 432 h and longer. For Al–Sc, the conductivity increases from $31.84 \pm 0.06 \text{ MS m}^{-1}$ as-homogenized to a plateau value of $36.44 \pm 0.08 \text{ MS m}^{-1}$. For Al–Li–Sc, conductivity similarly increases from $18.0 \pm 0.1 \text{ MS m}^{-1}$ to $19.33 \pm 0.05 \text{ MS m}^{-1}$. Also for Al–Li–Sc, a sharp decrease in conductivity to $17.0 \pm 0.1 \text{ MS m}^{-1}$ was observed at 60 s. This measurement was repeated on another aged specimen, but for the second measurement the decrease in conductivity was not observed. This is discussed in Section 4.1.

The Vickers microhardness values are displayed in Fig. 5a as a function of time at $325 \text{ }^\circ\text{C}$ of Al–Sc–Yb and the corresponding Al–Li–Sc–Yb alloy. For Al–Li–Sc–Yb, some specimens were double-aged, with a first heat treatment to peak microhardness at $325 \text{ }^\circ\text{C}$ for 2 h, followed by a second heat treatment at $170 \text{ }^\circ\text{C}$ for times from 24 to 1536 h. These double heat-treatments were used to induce precipitation of the α' - $\text{Al}_3(\text{Sc},\text{Li},\text{Yb})$ phase at $325 \text{ }^\circ\text{C}$ followed by precipitation of the metastable δ' - Al_3Li phase at $170 \text{ }^\circ\text{C}$ for a double-strengthening effect. Compared with the Yb-free alloys, these alloys exhibit much shorter incubation periods of $<1 \text{ min}$. Both alloys exhibit

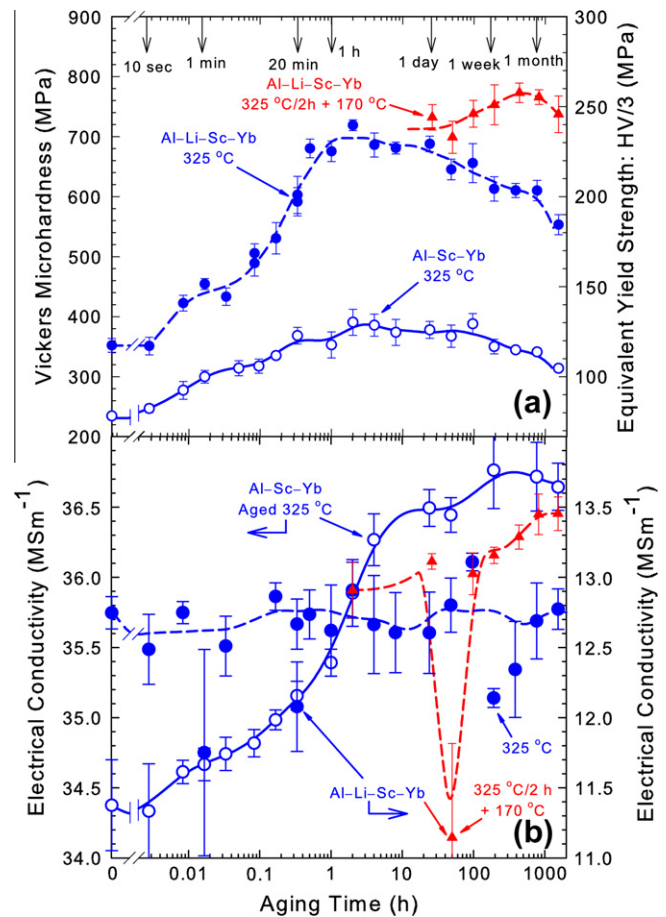


Fig. 5. (a) Vickers microhardness vs. aging time and (b) electrical conductivity vs. aging time for Al–Sc–Yb and Al–Li–Sc–Yb aged isothermally at $325 \text{ }^\circ\text{C}$, and for Al–Li–Sc–Yb aged isothermally for 2 h at $325 \text{ }^\circ\text{C}$, then aged isothermally at $170 \text{ }^\circ\text{C}$. Error bars correspond to 2SD (i.e., error range is 4SD).

trends in microhardness evolution similar to the Yb-free alloys (Fig. 4a). For Al–Sc–Yb, the plateau value of maximum microhardness is 376 ± 43 MPa, which is maintained between 20 min and 96 h, while for Al–Li–Sc–Yb the plateau value is larger: 688 ± 40 MPa, occurring between 0.5 and 24 h.

The electrical conductivities of Al–Sc–Yb and Al–Li–Sc–Yb are displayed in Fig. 5b as a function of aging time at 325 °C. Two different behaviors are observed. For Al–Sc–Yb, the homogenized and 10-s-aged specimens have the same conductivity, 34.4 ± 0.3 MS m⁻¹, whereafter the conductivity increases to its maximum value of 36.7 ± 0.3 MS m⁻¹ for > 192 h. The electrical conductivity of Al–Li–Sc–Yb does not evolve temporally during aging at 325 °C. The average conductivity during aging was 12.7 ± 0.4 MS m⁻¹. In general, conductivity measurements for this alloy were characterized by a high degree of scatter, both for measurements made on an individual specimen and from specimen-to-specimen. As explained, specimens of the Al–Li–Sc–Yb alloy were doubly-aged at 325 °C for 2 h, then for different durations at 170 °C. During aging at 170 °C, the conductivity decreases sharply after 48 h, recovers after 96 h, and then increases to a maximum value of 13.5 ± 0.1 MS m⁻¹ at 1536 h.

3.4. LEAP analysis of aged alloys

LEAP tomographic analyses were performed to investigate the aging microhardness responses. Analyses were performed on all alloys after aging at 325 °C to their peak-aged states: 2 h for the Yb-containing alloys, and 8 h for the Yb-free alloys. In addition, a series of analyses were performed on Al–Li–Sc for aging times of 0.16, 8, 24, 280 and 1536 h (Section 4.2.3). Fig. 1 shows a 3-D reconstruction of the Al–Sc–Yb alloy. Twenty α' -Al₃(Sc,Yb) precipitates, some of which are cut by the edge of the reconstructed volume, are visible in the data set. These are most visible in the reconstruction of Sc atoms, which partition strongly from the α -Al matrix to the α' -Al₃

(Sc,Yb) precipitates. Si and Yb atoms also partition to the α' -Al₃(Sc,Yb) precipitates, but the effect is less clear owing to their smaller concentrations, and also to the smaller S/N ratios for their peaks in a mass spectrum (Section 3.1), which makes it difficult to distinguish these ions from the background. Si and Yb also partition to linear features in the data set parallel to the tip axis. This is due to surface migration of these solutes to low-index poles (Section 3.1) and is an artifact of the LEAP tomographic technique for these alloys [46].

Phase compositions can be quantitatively measured by the proximity histogram (proxigram) technique [47]. A proxigram consists of first defining a surface of constant concentration (isoconcentration surface) in the reconstructed volume, which encloses the precipitated phase. The isoconcentration surfaces were defined as the surfaces of inflection of the Al concentration. Starting at an isoconcentration surface and moving into the α -Al matrix, the concentration of Al increases and assumes a far-field value. Starting at the isoconcentration surface and moving toward the center of the precipitate, the Al concentration decreases, and the solute concentrations increase. Using proxigram analyses, α' -Al₃(Sc,Li,Yb) and δ' -Al₃Li precipitates as well as α -Al matrix compositions were measured for the aged alloys (Table 2). Matrix concentrations are determined by summing atoms of each species in proxigram bins far from the isoconcentration surface (typically ~5 nm), in a region where the concentrations reach a stable far-field value. Precipitate concentrations are similarly determined by summing all atoms in bins interior to the isoconcentration surface.

Proxigrams are displayed in Fig. 6a and b for peak-aged (8 h at 325 °C) Al–Sc and Al–Li–Sc, respectively, and in Fig. 7a and b for peak-aged (2 h at 325 °C) Al–Sc–Yb and Al–Li–Sc–Yb, respectively. Concentrations were measured at distance increments of 0.1 nm. Phase compositions for the four alloys at aging times of interest are reported in Table 2. For the four alloys, all the solutes partition strongly from the α -Al matrix to the α' -Al₃(Sc,Li,Yb)

Table 2

Compositions of α' -Al₃(Sc,Li,Yb) precipitates (unshaded cells) and a δ' -Al₃Li precipitate (shaded cell) and the surrounding α -Al matrix in four Al(–Li)–Sc(–Yb) alloys after various heat treatments.

| Alloy | Aging time at 325 °C (h) | Matrix composition | | | | Precipitate composition (at.%) | | | |
|-------------|--------------------------|--------------------|-------------|-------------|--------------|--------------------------------|------------|-----------------|-------------|
| | | Li (at.%) | Sc (at.ppm) | Si (at.ppm) | Yb (at. ppm) | Li | Sc | Si | Yb |
| Al–Sc | 8 | – | 130 ± 30 | 74 ± 12 | – | – | 27.2 ± 0.3 | 0.64 ± 0.06 | – |
| Al–Li–Sc | 0.16 | 2.54 ± 0.06 | 630 ± 20 | 200 ± 10 | – | 8.8 ± 0.3 | 17.3 ± 0.5 | 0.49 ± 0.09 | – |
| | 8 | 2.51 ± 0.01 | 110 ± 20 | 44 ± 7 | – | 9.1 ± 0.2 | 17.0 ± 0.3 | 0.25 ± 0.04 | – |
| | 24 | 2.62 ± 0.02 | 49 ± 14 | 9 ± 6 | – | 8.1 ± 0.3 | 20.9 ± 0.4 | 0.04 ± 0.02 | – |
| | 280 | 2.53 ± 0.02 | 42 ± 17 | 9 ± 8 | – | 6.7 ± 0.1 | 21.4 ± 0.2 | 0.0009 ± 0.0008 | – |
| | 1536 | 2.45 ± 0.01 | 36 ± 7 | 34 ± 5 | – | 5.66 ± 0.06 | 21.5 ± 0.1 | 0.076 ± 0.009 | – |
| | ThermoCalc | 2.598 | 19 | – | – | 5.60 | 19.4 | – | – |
| Al–Sc–Yb | 2 | – | 170 ± 30 | 45 ± 18 | – | – | 27.2 ± 0.6 | 1.1 ± 0.1 | 2.7 ± 0.3 |
| Al–Li–Sc–Yb | 2 | 5.31 ± 0.01 | 75 ± 10 | 39 ± 5 | 12 ± 13 | 13.3 ± 0.2 | 10.1 ± 0.2 | 0.22 ± 0.03 | 2.03 ± 0.08 |
| | 2 + 192 h at 170 °C | 5.01 ± 0.02 | 110 ± 20 | 110 ± 10 | 1.5 ± 0.3 | 15.2 ± 0.4 | 10.9 ± 0.3 | 0.41 ± 0.07 | 1.7 ± 0.1 |
| | | | | | | 23.1 ± 0.7 | 0 | 0.007 ± 0.005 | 0 |

Values were determined by LEAP analysis of the aged alloys.

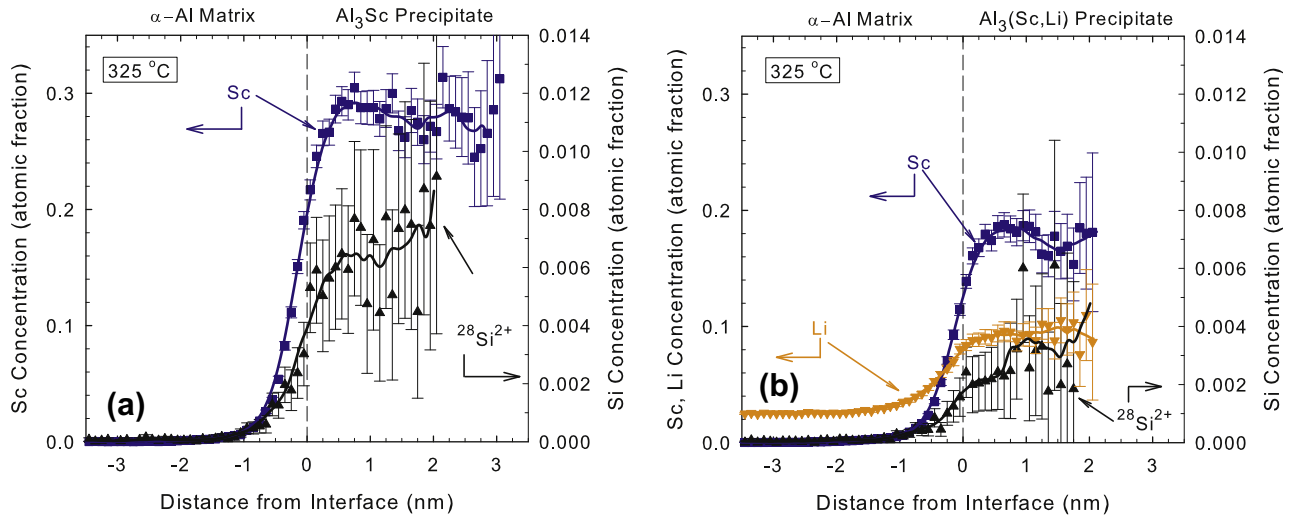


Fig. 6. Proximity histograms of precipitates in (a) Al–Sc and (b) Al–Li–Sc peak-aged at 325 °C for 8 h. Error bars correspond to 2SD (i.e., error range is 4SD).

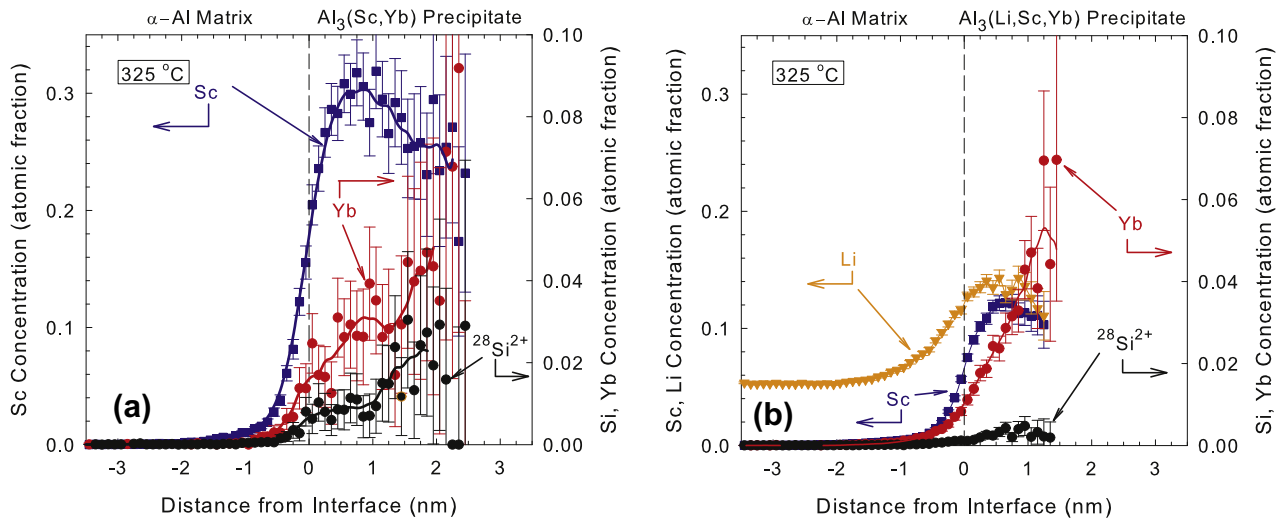


Fig. 7. Proximity histograms of precipitates in (a) Al–Sc–Yb and (b) Al–Li–Sc–Yb peak-aged at 325 °C for 2 h. Error bars correspond to 2SD (i.e., error range is 4SD).

precipitates. Li and Sc proxigrams from Al–Li–Sc aged at 325 °C for 0.16, 8, 24, 280 and 1536 h are displayed in Fig. 8 for Sc, Li and Sc + Li. As Al–Li–Sc aging progresses, the concentration of Sc increases, and the concentration of Li decreases in the α' -Al₃(Sc,Li) precipitates. These trends are displayed in Fig. 9, in which the concentrations of Sc and Li in the α' -Al₃(Sc,Li) precipitates are calculated using the proxigrams. Solute concentrations in the α -Al matrix for Al–Li–Sc aged for the times listed above, and for Al–Sc aged for 8 h, are displayed in Fig. 10.

Analysis of the 325 °C-aged alloys by LEAP tomography additionally allows measurement of several important characteristics of the α' -Al₃(Sc,Li,Yb) precipitates, which sheds light on the effect of Li additions on the microhardness response of the Al–Sc(–Yb) alloys. The number

density, average radius and volume fraction, for α' -Al₃(Sc,Li,Yb) precipitates in the aged alloys are given in Table 3. The volume fraction is calculated by isolating atoms in α' -Al₃(Sc,Li,Yb) precipitates using a modified envelope method [48], and dividing the number of α' -Al₃(Sc,Li,Yb) precipitate atoms by the total number of atoms in the reconstructed volume. The small difference in lattice parameters of the phases is accounted for by approximating the lattice parameter of the α' -Al₃(Sc,Li,Yb) precipitates to be that of α' -Al₃Sc (4.103 Å [49]), and the lattice parameter of the α -Al matrix to be that of Al–Li [50]. The number density is calculated by counting the number of α' -Al₃(Sc,Li,Yb) precipitates in the analyzed volume (precipitates cut by the boundary of the analysis volume are counted as half a precipitate), and dividing by the volume of material, which is inferred from the total

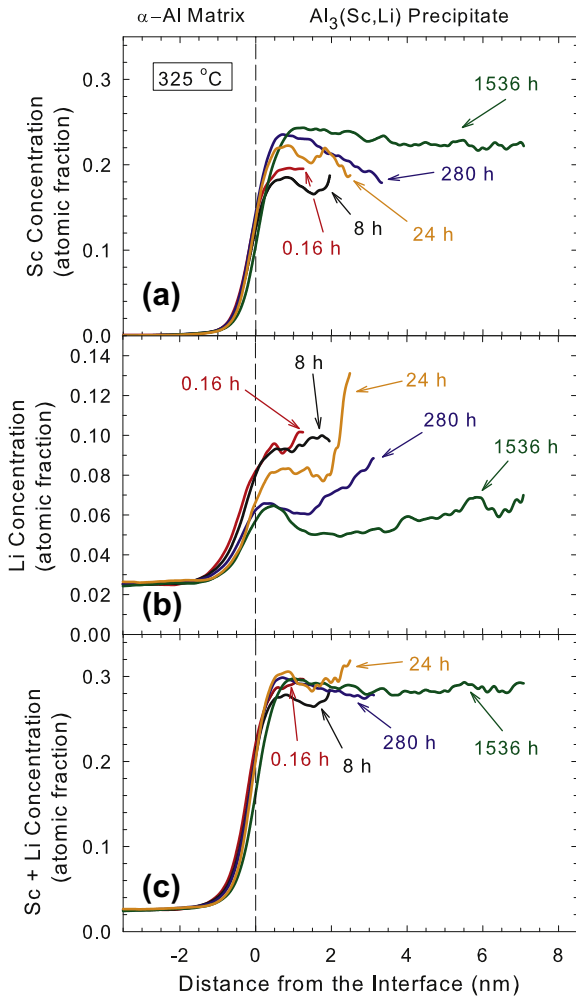


Fig. 8. Proximity histograms of precipitates in Al–Li–Sc aged at 325 °C for 0.16–1536 h for (a) Sc, (b) Li and (c) the sum of Sc and Li.

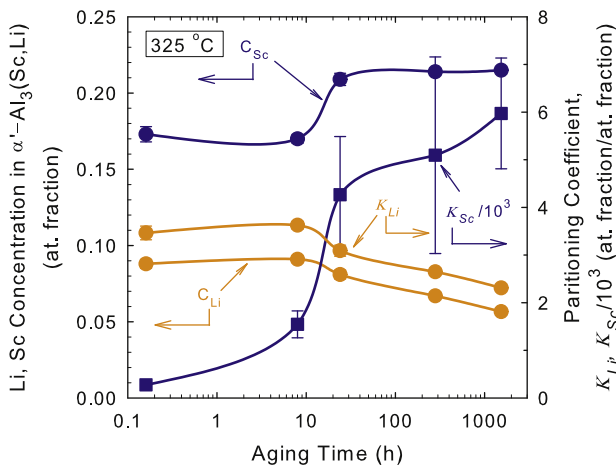


Fig. 9. Sc and Li concentrations in precipitates, and Sc and Li partitioning ratios in Al–Li–Sc aged at 325 °C.

number of atoms. The average radius is calculated from a precipitate size distribution (excluding precipitates cut by

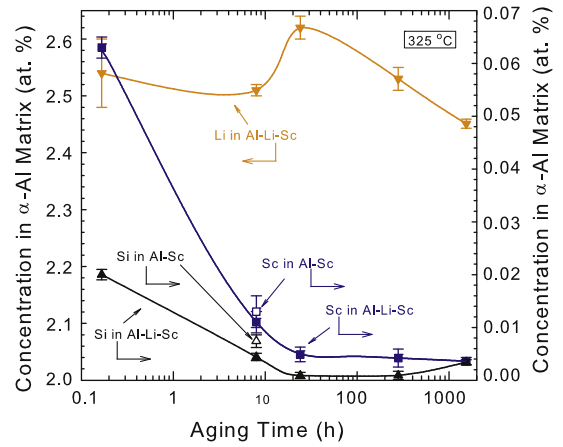


Fig. 10. Concentrations of Li, Sc and Si in the α -Al matrix as a function of aging time at 325 °C for Al–Li–Sc (a single point for 8 h aging is also shown for Al–Sc).

the boundary of the data set), obtained by applying a modified envelope method to the data sets [48], and approximating the α' - $\text{Al}_3(\text{Sc,Li,Yb})$ precipitates as volume-equivalent spheres. Standard methods for propagation of errors were employed for the quantities in Table 3 [51]. For Al–Li–Sc, these values are plotted as a function of aging time in Fig. 11.

Fig. 12 shows a LEAP reconstruction of Al–Li–Sc–Yb doubly-aged by first aging to peak hardness at 325 °C for 2 h, then at 170 °C for 8 days. This aging treatment was performed to induce precipitation of δ' - Al_3Li , which provides an additional strengthening increment [52–58]. Al–Li–Sc–Yb aged at 170 °C is the only alloy and aging treatment for which the Li concentration is anticipated to exceed its solubility for precipitation of metastable δ' - Al_3Li [59]; a similar heat treatment was not performed for Al–Li–Sc, because the Li concentration in that alloy (2.9 ± 0.1 at.%) is significantly smaller than the solvus for aging temperatures that would yield reasonable precipitation kinetics [60]. In Fig. 12, a 12 at.% Li isoconcentration surface delineates the α -Al/ δ' - Al_3Li interface and Sc atoms are indicated by blue points (Al and Li atoms are omitted for clarity). Yb atoms, which partition to the cores of Sc-rich precipitates as seen in singly-aged Al–Li–Sc–Yb (Fig. 7b), are also omitted for clarity because they appear to be nearly homogeneously distributed throughout the reconstructed volume due to the small S/N ratio (Section 3.1 and Fig. 2b). The metastable δ' - Al_3Li precipitate is elongated along the tip axis (vertical direction in Fig. 12), which is an artifact due to an inverse magnification of the δ' - Al_3Li precipitate [40,41]. The δ' - Al_3Li phase has a smaller evaporation field than the surrounding α -Al matrix, leading to depressions in the specimen surface at the δ' - Al_3Li precipitates during evaporation [61]. Also visible in Fig. 12 are six Sc-rich α' - $\text{Al}_3(\text{Sc,Li,Yb})$ precipitates, which are enclosed within a single metastable δ' - Al_3Li precipitate.

Table 3
Number density N_v , volume fraction ϕ and average radius $\langle R \rangle$ in four Al(-Li)-Sc(-Yb) alloys after various heat treatments.

| Alloy | Aging time at 325 °C (h) | Precipitate statistics | | |
|-------------|--------------------------|------------------------------------|-------------------|--------------------------|
| | | N_v (10^{22} m^{-3}) | ϕ (%) | $\langle R \rangle$ (nm) |
| Al-Sc | 8 | 5.0 ± 0.5 | 0.430 ± 0.003 | 2.7 ± 0.3 |
| Al-Li-Sc | 0.16 | 19.4 ± 0.1 | 0.292 ± 0.002 | 1.4 ± 0.3 |
| | 8 | 13.1 ± 0.1 | 0.557 ± 0.003 | 1.9 ± 0.4 |
| | 24 | 8.2 ± 0.7 | 0.478 ± 0.003 | 2.3 ± 0.4 |
| | 280 | 2.3 ± 0.3 | 0.433 ± 0.003 | 3.7 ± 0.7 |
| | 1536 | 0.6 ± 0.1 | 0.451 ± 0.002 | 5.2 ± 1.5 |
| Al-Sc-Yb | 2 | 1.5 ± 0.2 | 0.092 ± 0.001 | 2.7 ± 0.4 |
| Al-Li-Sc-Yb | 2 | 12.1 ± 0.7 | 0.401 ± 0.002 | 1.8 ± 0.4 |
| | 2 + 8 days at 170 °C | 10.4 ± 0.8 | 0.403 ± 0.002 | 1.5 ± 0.4 |

Values were determined by LEAP analysis of the aged alloys.

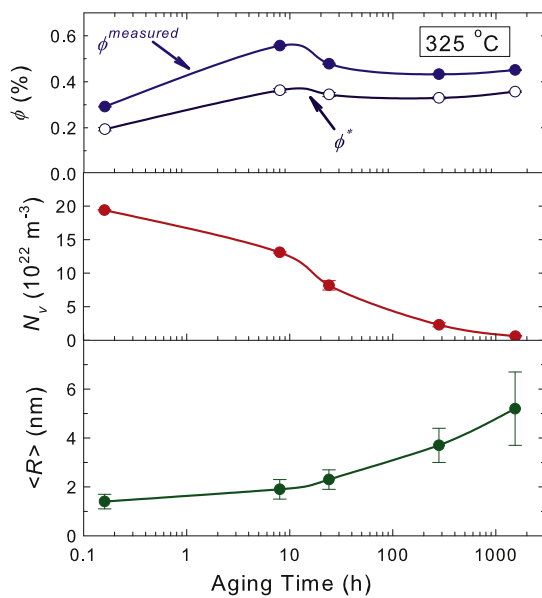


Fig. 11. The volume fraction (ϕ), number density (N_v) and average radius ($\langle R \rangle$) of precipitates in Al-Li-Sc during aging at 325 °C. Also shown in the top plot is ϕ^* , the volume fraction that would be present in a binary Al-Sc alloy if the precipitates contained no Li (see text for a complete description).

3.5. 5 Dark-field TEM of doubly-aged Al-Li-Sc-Yb

Owing to the small number density of metastable δ' -Al₃Li precipitates in doubly-aged Al-Li-Sc-Yb, very few were imaged by LEAP tomography. To access a larger field of view, the metastable δ' -Al₃Li precipitates produced by aging at 170 °C for 8 days after prior aging at 325 °C for 2 h, were imaged by centered dark-field TEM (DFTEM) (Fig. 13). Superlattice reflections in the selected-area diffraction patterns indicated that the metastable δ' -Al₃Li precipitates have an L1₂ structure. The micrograph in Fig. 13 was taken along a [2 1 0] zone axis and imaged using a 0 0 1 superlattice reflection. Precipitate radii were measured using the particle analysis feature in Image J, after thresholding the images to select the precipitated phase. By adjusting the threshold values for pixel inclusion in the precipitates, the value found for average precipitate radius also changes. Across the range of threshold values that

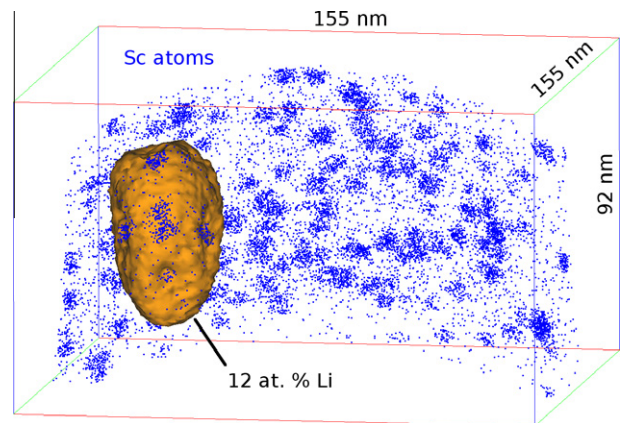


Fig. 12. LEAP reconstruction of Al-Li-Sc-Yb aged for 2 h at 325 °C, then for 8 days at 170 °C. Sc atoms are shown as blue points, regions where Sc atoms are concentrated correspond to α -Al₃(Sc,Li,Yb) precipitates. Shown in orange is a 12 at.% Li isoconcentration surface corresponding to a δ' -Al₃Li precipitate containing six α' -Al₃(Sc,Li,Yb) precipitates. (For interpretation of the references to colour in this figure legend, the reader is referred to the web version of this article.)

clearly separate precipitates from the matrix, the value found for the average radius varies by $\sim \pm 0.6$ nm. Using the center of the threshold range thus determined, the average radius for 304 metastable δ' -Al₃Li precipitates imaged by this method is 16.8 ± 5.7 nm. Here the value 5.7 nm is a measure of the breadth of the precipitate size distribution, rather than an experimental error, which is about ± 0.6 nm as described above.

4. Discussion

4.1. Evolution of the α -Al matrix compositions

The electrical conductivities of Al-Li-Sc and Al-Li-Sc-Yb decrease significantly at or near the onset of microhardness increases in both isochronal (Fig. 3b) and isothermal aging (Figs. 4b and 5b), including during isothermal aging of Al-Li-Sc-Yb at 170 °C. The decrease in conductivity is especially strong in Al-Li-Sc-Yb, which has a higher Li concentration than Al-Li-Sc. These observations suggest that this decrease is related to a nucleation event in

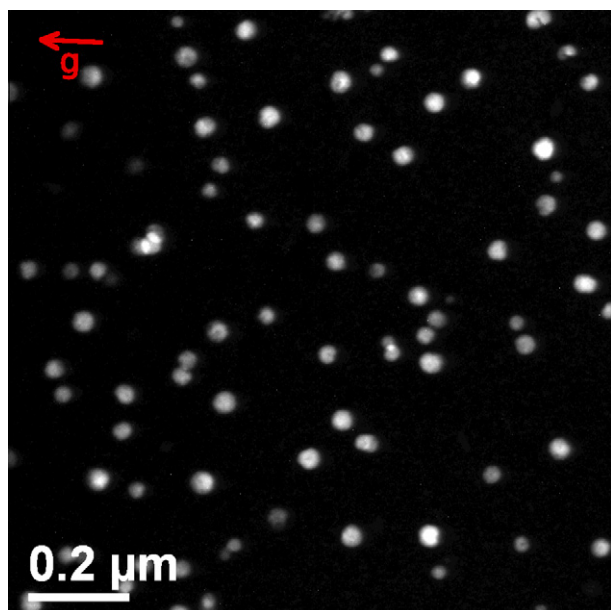


Fig. 13. Centered DFTEM micrograph showing metastable δ' - Al_3Li precipitates in Al–Li–Sc–Yb aged for 2 h at 325 °C, then for 8 days at 170 °C. The image is taken along $[2\ 1\ 0]$ zone axis using the $0\ 0\ 1$ superlattice reflection.

Li-containing alloys. This effect has been demonstrated in studies on binary Al–Li alloys by low-temperature isothermal aging experiments (40–130 °C) [59,62–65], and was shown to be due to ordering of the alloy into Li-rich, Li_2 -ordered domains, or metastable δ' - Al_3Li precipitates. A decrease in conductivity at early aging times and low temperatures has been similarly observed in a number of other binary Al alloys as well as in Al–Li [66], and is generally attributed to a large number density of solute atom clusters. Furthermore, it has been shown analytically that the mechanism of conductivity decrease in the early stages of aging in a binary alloy can be attributed to Bragg scattering from Guinier–Preston (G–P) zones, which are present at a large number density [67].

The electrical conductivity of the 99.999% pure source Al is $37.3 \pm 0.1 \text{ MS m}^{-1}$. Conductivities of homogenized Al–Li–Sc and Al–Li–Sc–Yb are smaller ($18.0 \pm 0.1 \text{ MS m}^{-1}$ and $12.7 \pm 0.4 \text{ MS m}^{-1}$, respectively; Figs. 4 and 5), primarily due to the presence of solute atoms that scatter electrons. To understand the effects of solutes on alloy conductivity, it is necessary to quantify the contribution of solute atoms to electron scattering. Normalized to solute concentration, this is the specific resistivity of a solute dissolved in the matrix. The specific resistivity of Li dissolved in Al was reported to be $9.2 \text{ n } \Omega \text{ m at.}\%^{-1}$ [62] or $8.4 \text{ n } \Omega \text{ m at.}\%^{-1}$ [63]. The specific resistivity of Sc in Al was given in the literature as $34 \text{ n } \Omega \text{ m at.}\%^{-1}$ [68] or $35 \text{ n } \Omega \text{ m at.}\%^{-1}$ [69]. These values permit the increases in conductivity (Figs. 3b, 4b and 5b) to be interpreted in terms of depletion of the matrix solute concentrations, as demonstrated below.

The average conductivity of Al–Li–Sc–Yb during isothermal aging at 325 °C is $12.6 \pm 0.1 \text{ MS m}^{-1}$. Accounting

only for the LEAP tomographic measurements of Li concentration in this alloy, and taking the contributions in resistivity from solute additions to the pure Al matrix to be linearly additive (Mathiessen's rule [70]), the conductivity of the alloy would be 13.1 MS m^{-1} . Similarly, the conductivity of a hypothetical Al–Sc solid solution with the Sc concentration of Al–Li–Sc–Yb (0.0506 at.%) would be 35.0 MS m^{-1} . An Al–5.612Li–0.0506Sc (at.%) solid solution should have a conductivity value of 12.8 MS m^{-1} , in good agreement with the measured value. Although the specific resistivity of Sc atoms in Al solid solution is greater than that of Li atoms, the electrical conductivity behavior is controlled by the Li concentration in solid solution, because the Li concentrations and concentration changes during aging of these alloys are much greater than those of Sc. For isothermally aged Al–Li–Sc–Yb, the only aging treatment for which the conductivity response is larger than the measurement uncertainty is for the second aging treatment at 170 °C. This is because the change in Li concentration in the matrix during aging at 325 °C is small compared with the total Li concentration of 5.53 at.%; for example, the change in Li concentration, estimated from measurements of the precipitate number density and Li concentration of α' - $\text{Al}_3(\text{Sc}, \text{Yb}, \text{Li})$ after aging for 2 h is $\sim 0.03 \text{ at.}\%$. The sharp decrease in conductivity after aging at 170 °C for 2 days is most likely due to the early stages of metastable δ' - Al_3Li formation, as reported for various Al–Li alloys aged at 40–400 °C, depending on Li concentration [59,62,65]. With further aging, the conductivity recovers and increases, indicating that the metastable δ' - Al_3Li precursor domains have become metastable δ' - Al_3Li precipitates at a smaller number density, and the matrix is becoming depleted in Li. In this manner, the conductivities of the aged alloys can be correlated with precipitate nucleation, and with the evolution of the matrix's solute concentration, as measured by LEAP.

Similar calculations on the other alloys yield the following results: the conductivity of Al–Sc is calculated to increase from 31.4 MS m^{-1} as-homogenized to 37.2 MS m^{-1} at long aging times (31.84 ± 0.06 – $36.44 \pm 0.08 \text{ MS m}^{-1}$ was measured); the conductivity of Al–Li–Sc is calculated to increase from 18.6 to 20.6 MS m^{-1} (18.0 ± 0.1 to $19.33 \pm 0.05 \text{ MS m}^{-1}$ was measured); and the conductivity of Al–Sc–Yb is calculated to increase from 35.0 to 37.2 MS m^{-1} (34.4 ± 0.3 to $36.7 \pm 0.3 \text{ MS m}^{-1}$ was measured).

One study was performed on phase equilibria in the Al–Li–Sc system (0–41 at.% Li and 0–53 at.% Sc) [71,72], but it is of limited relevance to our research, since the concentration range of interest was not explored in detail. Otherwise, ternary and higher phase diagrams are unavailable for this system. At 170 °C, the solubility of Li in α -Al is 5.39 at.% [59]. The concentration of Li in solution in the α -Al matrix decreases from $5.31 \pm 0.01 \text{ at.}\%$ after aging for 2 h at 325 °C, to $5.01 \pm 0.02 \text{ at.}\%$ after additional aging for 8 days at 170 °C (Table 2), demonstrating that the addition of Sc, Si, and Yb decreases the solubility of Li in Al.

The electrical conductivity of Al–Li–Sc is constant for aging times of 384 h (16 days) and longer, suggesting that α -Al and α' -Al₃(Sc,Li) precipitates are close to equilibrium for these solute concentrations at 325 °C. In Al–Li–Sc, the equilibrium solubility of Sc in α -Al (36 ± 7 at. ppm) is therefore close to the equilibrium solubility of Sc in binary Al–Sc, determined by a linear fit to the data in Ref. [49] to be 14 at.ppm. The α -Al's Li concentration after 1536 h is 2.449 ± 0.005 at.%; hence this Li concentration does not appear to decrease the solubility of Sc in α -Al.

The presence of Si impurity atoms in α -Al has been shown to affect the temporal evolution of the microstructure, resulting in a significant increase in strength in aged commercial-purity (Si-containing) Al–Sc alloys relative to aged high-purity Al–Sc alloys [73]. In Al–Li–Sc, the concentration of Si in the α -Al matrix decreases during aging at 325 °C (Table 2 and Fig. 10). Although the measurement of Si concentration is subject to a degree of error, as noted above, this decreasing trend corresponds to partitioning of Si to the precipitates as discussed in the following section.

4.2. Strengthening precipitates in the aged alloys

4.2.1. Precipitate compositions in peak-aged alloys

The compositions of α' -Al₃(Sc,Li) precipitates in Al–Li–Sc and Al–Sc aged 8 h at 325 °C were measured using proxigrams (Fig. 6), and are reported in Table 2. The α' -Al₃Sc precipitates in Al–Sc have approximately the Al₃Sc stoichiometry, 27.2 ± 0.3 at.% Sc. A Sc concentration greater than the 25 at.% stoichiometric value at early aging times is consistent with prior measurements on similar alloys [16–17,20–21,73]. The precipitates also contain 0.64 ± 0.06 at.% Si. The presence of 20–30 at.% Sc and ~ 6 at.% Si was reported in the centers of precipitates observed in Al–0.096Sc–0.048Si (at.%) aged at 300 °C [74]. Results of a first-principles study [74] on the site occupancy of a Si atom in Al₃Sc demonstrate that Si resides on the Al-sublattice, resulting in an (Al,Si)₃Sc phase. The proxigrams (Figs. 6 and 7) demonstrate that Si partitions strongly to the precipitate in which the distribution of Si is uniform, following the same concentration profile as Sc. The precipitates in Al–Li–Sc aged for 8 h at 325 °C contain 17.0 ± 0.3 Sc, 9.1 ± 0.2 Li and 0.25 ± 0.04 Si (at.%). The combined Sc + Li concentration is 26.1 ± 0.4 at.%, which is similar to the Sc concentration in peak-aged Al–Sc (27.2 ± 0.3 at.%). This suggests that Li substitutes for Sc in Al₃Sc, resulting in a precipitate with the stoichiometry (Al,Si)₃(Sc,Li). That result is counter to the results of a study of the phase equilibria in Al–Li–Sc, where no ternary compounds were reported [71,72]. However, for two alloys (Al–8.0Li–0.3Sc and Al–7.3Li–2.3 Mg–0.3Sc (at.%)), which were cast and rolled at 500 °C, primary precipitates measuring several micrometers were found to have the L1₂ structure, and approximately the same lattice parameter as the α -Al matrix [37,38]. Auger spectroscopy showed that these precipitates, which formed on solidification from the melt, have a composition Al₃(Li_xSc_{1-x}), where $x \geq 0.5$

[37]. This is in agreement with the nanometer-sized precipitates formed through solid-state precipitation in the present research and in studies on Al–Li–Sc and Al–Li–Sc–X alloys [36,39–41].

Similar analyses were performed for precipitates in Al–Li–Sc and Al–Li–Sc–Yb aged to peak microhardness for 2 h at 325 °C (Fig. 7 and Table 2). All solute elements in both alloys partition strongly to the α' -Al₃(Sc,Li,Yb) precipitates, and Yb is found at the highest concentrations toward the center of the precipitates, with the Sc concentration peaking toward the α -Al matrix/ α' -Al₃(Sc,Li,Yb) precipitate interface, corresponding to the core/shell structure for Al–Sc–RE [16–17,75] and Al–Li–Sc–Yb alloys [40,41]. In both alloys, Si partitions to the α' -Al₃(Sc,Li,Yb) precipitates.

Because of the difficulties described earlier in measuring Si concentrations (migration of Si atoms over the specimen surface during LEAP analysis, and small Si concentrations), only qualitative statements can be made regarding Li additions and Si partitioning. For all four alloys in the peak-aged state, the degree of partitioning of Si to the α' -Al₃(Sc,Li,Yb) precipitates decreases with the Li addition. For Al–Sc–Yb, the partitioning ratio of Si (defined as the ratio of Si concentration in the α' -phase to that of Si in the α -Al matrix) decreases from 240 ± 100 to 56 ± 11 with Li addition; for Al–Sc it similarly decreases from 86 ± 16 to 57 ± 13 . Since Li replaces Sc in the precipitated phase, it is unclear whether the incorporation of Li into α' -Al₃(Sc,Li,Yb) impedes Si partitioning or whether Si partitioning depends on the presence of Sc, whose concentration is reduced with the Li addition. The partitioning coefficients of Sc in the peak-aged alloys are also somewhat reduced due to Li additions: for peak-aged Al–Sc, the partitioning coefficient of Sc decreases with Li addition from 2090 ± 480 to 1550 ± 280 ; and similarly for Al–Sc–Yb it decreases from 1600 ± 300 to 1350 ± 180 . This is in agreement with the observation that Li displaces Sc in the α' -Al₃(Sc,Li,Yb) precipitates. Although the precipitation reaction is faster in Al–Li–Sc than in Al–Sc, the partitioning ratio of Sc is reduced by Li addition.

4.2.2. α' -Al₃(Sc,Li,Yb) precipitate statistics in the peak-aged state

Statistics to characterize the α' -Al₃(Sc,Li,Yb) precipitates in the aged alloys, as measured by analyzing reconstructed LEAP volumes, are reported in Table 3. The addition of Li to Al–Sc and to Al–Sc–Yb induces changes in the distribution of α' -Al₃(Sc,Li,Yb) precipitates during aging at 325 °C. After aging for 8 h, the α' -Al₃(Sc,Li) precipitates in Al–Li–Sc are smaller than those in Al–Sc (1.9 ± 0.4 nm vs. 2.7 ± 0.3 nm), and have a higher number density ($13.1 \pm 0.1 \times 10^{22} \text{ m}^{-3}$ vs. $5.0 \pm 0.5 \times 10^{22} \text{ m}^{-3}$). These values suggest a greater nucleation current and a smaller energy barrier for nucleation, although the nucleation event has not been directly observed by microscopy. The volume fraction is somewhat smaller in Al–Sc ($0.430 \pm 0.003\%$) than in Al–Li–Sc ($0.557 \pm 0.003\%$),

owing to the presence of Li in the $\text{Al}_3(\text{Sc,Li})$ precipitates. An Al–Sc alloy with the Sc concentration of an Al–Li–Sc alloy aged for 8 h (0.1138 ± 0.0013 at.%) should exhibit an equilibrium volume fraction of $0.467 \pm 0.005\%$, based on the lever rule. The addition of 2.9 at.% Li to Al–0.11 at.% Sc alloy increases the volume fraction of α' - $\text{Al}_3(\text{Sc,Li})$ precipitates in the peak-aged alloy by $\sim 30\%$.

Based on LEAP tomographic analyses, neither Al–Sc nor Al–Li–Sc was observed to be in thermodynamic equilibrium after aging for 8 h at 325°C . The solid solubility of Sc in Al at 325°C is 0.0014 at.% [49], and for a Sc concentration of 0.1450 ± 0.0018 at.% (LEAP tomography value, Table 1), an equilibrium volume fraction of $0.597 \pm 0.007\%$ is anticipated in a binary Al–Sc alloy at equilibrium at 325°C . Hence, the precipitation reaction is $\sim 70\%$ complete after 8 h and, although the strength of Al–Sc decreases for longer aging durations, the growth period of the decomposition reaction remains incomplete, and a larger volume fraction of α' - Al_3Sc is anticipated at later aging times. Al–Li–Sc also continues to evolve significantly between 1/3 and 64 days, as described in Section 4.2.3.

Li additions to Al–Sc–Yb similarly affect the α' - $\text{Al}_3(\text{Sc,Li,Yb})$ precipitate population in the alloy peak-aged for 2 h at 325°C . Compared with Al–Sc–Yb, α' - $\text{Al}_3(\text{Sc,Li,Yb})$ precipitates in Al–Li–Sc–Yb are smaller (1.8 ± 0.4 vs. 2.7 ± 0.4 nm) and the number density is almost one order of magnitude larger ($12.1 \pm 0.7 \times 10^{22} \text{ m}^{-3}$ vs. $1.5 \pm 0.2 \times 10^{22} \text{ m}^{-3}$). Similarly to the Yb-free alloys, a Li addition increases the volume fraction in the peak-aged alloys from $0.092 \pm 0.001\%$ to $0.401 \pm 0.002\%$. Although the Al–Sc–Yb phase diagram has not been determined, if all the Sc and Yb in Al–0.048Sc–0.0092Yb (at.%) were to precipitate as α' - $\text{Al}_3(\text{Sc,Yb})$ precipitates, the maximum achievable volume fraction would be 0.24% . The addition of 5.53 at.% Li to Al–0.048Sc–0.0092Yb (at.%), therefore, increases the volume fraction in the peak-aged alloy by $\sim 70\%$ over the maximum value achievable in a Li-free alloy.

4.2.3. Evolution of α' - $\text{Al}_3(\text{Sc,Li})$ precipitates in Al–Li–Sc

A striking feature of the Al–Li–Sc proxigrams (Fig. 8b) is the marked interfacial segregation of Li that develops for long aging times at the α -Al/ α' - $\text{Al}_3(\text{Sc,Li})$ interface, in particular at 1536 h. Solute segregation at a heterophase interface in a ternary alloy is quantifiable using the Gibbs adsorption isotherm [19,20,76–81]. The Gibbsian interfacial excess of Li relative to Sc and Al is expressed by [82,83]:

$$\begin{aligned} \Gamma_{\text{Li}}^{\text{Al-Sc}} &= \Gamma_{\text{Li}} - \Gamma_{\text{Sc}} \frac{c_{\text{Al}}^{\alpha} c_{\text{Li}}^{\alpha'} - c_{\text{Al}}^{\alpha'} c_{\text{Li}}^{\alpha}}{c_{\text{Al}}^{\alpha} c_{\text{Sc}}^{\alpha'} - c_{\text{Al}}^{\alpha'} c_{\text{Sc}}^{\alpha}} - \Gamma_{\text{Al}} \frac{c_{\text{Li}}^{\alpha} c_{\text{Sc}}^{\alpha'} - c_{\text{Li}}^{\alpha'} c_{\text{Sc}}^{\alpha}}{c_{\text{Al}}^{\alpha} c_{\text{Sc}}^{\alpha'} - c_{\text{Al}}^{\alpha'} c_{\text{Sc}}^{\alpha}} \\ &= - \left(\frac{\partial \gamma}{\partial \mu_{\text{Li}}} \right)_{T,P,\mu_{\text{Al}},\mu_{\text{Sc}}} \end{aligned} \quad (1)$$

where the c_i^j are the concentrations of component i in phase j (in this notation, the superscript α indicates the α -Al matrix phase, and α' indicates the α' - $\text{Al}_3(\text{Sc,Li})$ precipitate

phase), γ is the interfacial free energy of the α -Al matrix/ α' - $\text{Al}_3(\text{Sc,Li})$ interface, and μ_i is the chemical potential of component i . The excess concentration of the i th component Γ_i , determined from the proxigrams analysis, is given by [84]

$$\Gamma_i = \rho \Delta x \sum_{m=1}^p (c_i^m - c_i^k) \quad (2)$$

where ρ is the atomic density, Δx is the distance between p layers in the proxigram, and c_i^k is the concentration of component i in phase k , where k indicates the phase in which the proxigram is considered for each of its data points. Values of $\Gamma_{\text{Li}}^{\text{Al-Sc}}$ for each aging time are displayed in Fig. 14. Its value is positive for all aging times (indicating an excess of Li), and it is largest at 1536 h, indicating that the relative interfacial excess is most likely an equilibrium condition, validating this approach [76,82,83]. The differential form of the Gibbs adsorption isotherm, at constant temperature and pressure, yields a relationship between the relative interfacial excesses and the interfacial energies. Starting from Eq. (1), employing only the first-order dependence on concentration, one obtains for the change in interfacial free energy, $\Delta\gamma$ [76,79,82,83]:

$$\Delta\gamma|_{T,P} = -\Gamma_{\text{Li}}^{\text{Al-Sc}} \left(\frac{\partial \mu_{\text{Li}}}{\partial c_{\text{Li}}} \right) c_{\text{Li}} \quad (3)$$

The differential of chemical potential with respect to concentration, $\partial \mu_{\text{Li}} / \partial c_{\text{Li}}$ is evaluated by two methods: (i) making the ideal solution approximation; and (ii) using Thermo-Calc Classic version R (TCCR, Thermo-Calc Software) with the TTAL7 database (Thermotech Ltd., Guildford, UK). For Al–2.9Li–0.106Sc (at.%) at 325°C , the molar fractions and compositions of the α -Al matrix and α' - $\text{Al}_3(\text{Sc,Li})$ precipitates calculated by ThermoCalc with the TTAL7 database are relatively close to the measurements made at 1536 h (Table 2), implying that the thermodynamic properties at long aging times are reasonably well described. After aging for 1536 h, $\Gamma_{\text{Li}}^{\text{Al-Sc}} = 2.60 \pm 0.01$ atom nm^{-2} , the decrease in the interfacial free energy due

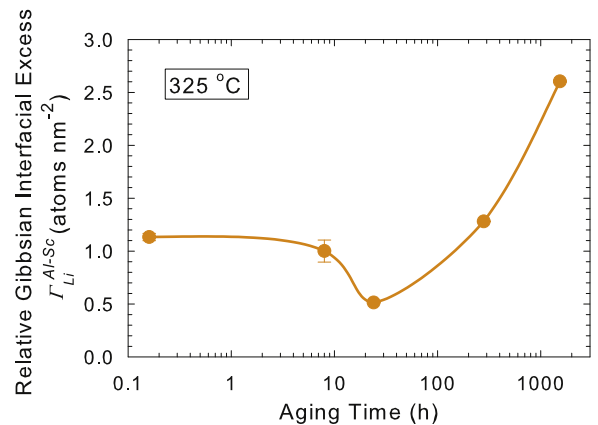


Fig. 14. Relative Gibbsian interfacial excess of Li ($\Gamma_{\text{Li}}^{\text{Al-Sc}}$) at the α -Al matrix/ α' - $\text{Al}_3(\text{Li,Sc})$ precipitate interface in Al–Li–Sc aged at 325°C .

to segregation is $\Delta\gamma = -22.7 \pm 0.1 \text{ mJ m}^{-2}$ using the ideal solution approximation, or $\Delta\gamma = -24.4 \pm 0.1 \text{ mJ m}^{-2}$ using results from Thermocalc. For reference, the interfacial excesses compare to $\Gamma_{Mg}^{Al-Sc} = 1.9 \pm 0.5 \text{ atom nm}^{-2}$ in an Al–2.2 Mg–0.12Sc (at.%) alloy aged at 300 °C [28]. The values for the reduction in interfacial free energy are large compared with the α -Al/Al₃Sc interfacial free energy in the binary Al–Sc system, found from coarsening studies to be between 20 and 300 mJ m⁻² [68,85–90]. Because the rate constant for precipitate coarsening in ternary alloys varies linearly with the interfacial free energy [91], using the larger value, 300 mJ m⁻², the interfacial excess reduces the rate of increase in $\langle R \rangle^3$ by 8% for an averaged value of $\Delta\gamma = -23.5 \text{ mJ m}^{-2}$.

A significant concentration of Li in α' -Al₃(Sc,Li) is produced during aging at 325 °C (~6–9 at.%, depending on aging time; Table 2), although in the binary Al–Li system at this same temperature, a Li concentration of 2.9 at.% is insufficient to produce δ' -Al₃Li precipitates [59]. To understand the mechanisms for this behavior, Mao et al. performed first-principles calculations on the Al–Li–Sc system [92], which yield insights into its precipitation behavior. They show that Li and Sc share the same sublattice site in the L1₂ structure and that it is energetically favorable for Li in solution in α -Al to partition to Al₃Sc and substitute for Sc. The inverse reaction, partitioning of Sc from α -Al substituting for Li in Al₃Li, is also energetically possible. Furthermore, the energetics are favorable if the substituted element forms additional trialuminide phase (rather than being rejected into the α -Al), thereby increasing the volume fraction. These results suggest that the presence of a mixed ternary Al₃(Sc,Li) trialuminide phase is a snapshot of the Al–Li–Sc system evolving temporally toward equilibrium as opposed to a transient, kinetically favored state only.

The temporal evolution of precipitate volume fraction, number density and average radius of Al–Li–Sc at 325 °C are displayed in Fig. 11. For comparison, a parameter φ^* is also shown in the plot of volume fraction, where φ^* is defined as the volume fraction of precipitates that would be present if the precipitates did not contain Li atoms. In other words, the quantity φ^* is calculated by counting all Sc atoms that partition to α' -Al₃(Sc,Li) precipitates, then computing the corresponding volume of stoichiometric α' -Al₃Sc, assuming a lattice parameter of 4.103 Å [49]. Therefore, although additions of both Li and Mg lead to solid-solution strengthening of the α -Al matrix, only Li, due to its high solubility in α' -Al₃Sc (not exhibited by Mg [29]) produces the additional benefit of increasing the volume fraction of precipitates and hence also increasing the strengthening increment of the peak-aged alloy [30].

Although the number density decreases, and the average radius increases with time, as anticipated for a system approaching equilibrium, the volume fraction evolves in an unexpected manner, increasing initially to a maximum value of $0.557 \pm 0.003\%$ at 24 h, followed by a decrease at longer aging times to a value of $0.451 \pm 0.002\%$ at

1536 h. This behavior may be understood by considering the concentration of Li in the α' -Al₃(Sc,Li) precipitates (Table 2 and Figs. 8 and 9). Excluding the earliest aging time of 0.16 h, the concentration of Li in the α' -Al₃(Sc,Li) precipitates is continuously decreasing during aging. The large volume fraction at 8 h is due to a high level of incorporation of Li in α' -Al₃(Sc,Li), forming precipitates with the approximate composition Al_{0.739}(Sc_{0.170}Li_{0.091}) at early aging times. The degree of elevated Li concentration is a transient condition as the concentration of Li in the α' -Al₃(Sc,Li) precipitates decreases during aging to Al_{0.728}(Sc_{0.235}Li_{0.056}) at 1536 h, with a concomitant decrease in volume fraction and partitioning ratio of Li.

An explanation for the large concentration of Li in the α' -Al₃(Sc,Li) precipitates at early aging times is that a positive Gibbsian relative excess of Li at the α -Al/ α' -Al₃(Sc,Li) interface is measured. Interfacial segregation of Li decreases the Gibbs free energy of the α -Al/ α' -Al₃(Sc,Li) interface. The net reversible work to form a nucleus of critical radius $R^* = 2\gamma/(\Delta F_{ch} - \Delta F_{el})$ is given by $W^* \approx (16\pi\gamma^3)/[3(\Delta F_{ch} - \Delta F_{el})^2]$ [93,94], where ΔF_{ch} is the chemical component of the Helmholtz free energy per unit volume due to a solute supersaturation at 325 °C, and ΔF_{el} is the elastic strain energy expended for nucleation of precipitates having a lattice parameter misfit with the matrix. Using Thermocalc and the TTAL7 database, which provide a qualitative comparison of the chemical driving force for precipitation, ΔF_{ch} at 325 °C is 4.715 kJ mol⁻¹, compared with 4.108 kJ mol⁻¹ for Al–Sc with the same Sc concentration. Because the lattice parameter mismatch of α' -Al₃Sc with α -Al is 1.32% [49,95], and the lattice parameter mismatch of δ' -Al₃Li with α -Al is -0.99% [95,96], it is anticipated that Li-incorporation in the α' -Al₃Sc precipitates results in a reduction in the lattice parameter mismatch, and hence a reduction in the elastic strain energy of a nucleus. Since the nucleation current is proportional to $\exp(-W^*/k_B T)$ [93,94], three factors may be identified that lead to a decrease in the critical radius and an increase in the nucleation current with addition of Li to binary Al–Sc: (i) the decrease in the interfacial free energy due to segregation of Li at the α -Al/ α' -Al₃(Sc,Li) interface; (ii) the increase in the chemical driving force for nucleation due to Li; and (iii) a decrease in the elastic strain energy of forming a nucleus. As a consequence, the incubation time for the microhardness response is reduced with the Li addition from 10 min in Al–Sc to 2 min in Al–Li–Sc. The average radius is smaller and the number density is larger in peak-aged (8 h) Al–Li–Sc compared with Al–Sc (Table 3). Because a small decrease in interfacial free energy γ results in a large decrease in the net reversible work to form a critical radius (proportional to γ^3), nuclei with a positive excess of Li are strongly favored.

At longer aging times, when nucleation is complete, the conditions leading to smaller radii of the critical nucleus (smaller interfacial energy, larger chemical driving force for nucleation, smaller lattice parameter mismatch) no longer control the concentration of solutes in the

precipitates, which evolve temporally toward their equilibrium chemical composition. Hence, for long aging times, the Li concentration decreases (from ~ 9 at.% at early aging times to ~ 6 at.% at long aging times), leading to a concomitant decrease in the volume fraction, as described above and demonstrated by Table 3 and Fig. 11.

4.2.4. Metastable δ' -Al₃Li in double-aged Al–Li–Sc–Yb

For Al–Li–Sc–Yb, the second aging step of 8 days at 170 °C has little effect on the precipitates formed during aging for 2 h at 325 °C, in terms of both the statistical metrics (Table 3) and their compositions (Table 2). The additional microhardness increment at 170 °C, from 719 ± 9 MPa to 773 ± 16 MPa is due to the formation of metastable δ' -Al₃Li, which nucleated heterogeneously on the α' -Al₃(Sc,Li,Yb) precipitates formed at 325 °C, as illustrated in Fig. 12. As described above, a δ' -Al₃Li precipitate has enveloped six Sc-rich α' -Al₃(Sc,Li,Yb) precipitates. A similar observation was made in Ref. [41] for an Al–6.3Li–0.069Sc–0.018Yb (at.%) alloy aged at 325 °C for 8 h, followed by quenching to 170 °C and aging for 1 week, which reported an instance where two α' -Al₃(Sc,Li,Yb) precipitates were enveloped by a single metastable δ' -Al₃Li precipitate. The composition of the δ' -Al₃Li precipitate is 23.1 ± 0.7 at.% Li and 70 ± 50 at. ppm Sc, which compares to a Li concentration in δ' -Al₃Li of 22.5 at.% at 170 °C, based on a Calphad-type study of the Al–Li system [97].

The concentration of Li in the alloy, 5.53 at.%, which was reduced from 6.3 at.% in an Al–6.3Li–0.069Sc–0.018Yb (at.%) alloy in Refs [40,41], is small enough to avoid grain-refining primary precipitates, which were observed in that alloy. However, owing to the large concentration of Li that can be dissolved in α -Al (5.38 at.% in a binary Al–Li alloy at 170 °C [59]) a Li concentration of 5.53 at.% is too small to yield significant strengthening due to metastable δ' -Al₃Li precipitation: the volume fraction of δ' -Al₃Li precipitates is estimated to be $1.4 \pm 0.1\%$ based on the decrease in the α -Al matrix concentration of Li during aging 192 h at 170 °C (Table 2). This establishes a rather narrow range of acceptable Li concentrations to achieve: (i) high-strength at ambient temperature for a doubly-aged alloy containing both α' -Al₃(Sc,Yb,Li) precipitates from aging at ~ 325 °C and metastable δ' -Al₃Li precipitates from aging at 170 °C; and (ii) creep resistance for a coarse-grained alloy containing only α' -Al₃(Sc,Yb,Li) precipitates after a single-temperature aging at 325 °C.

5. Summary and conclusions

Two Al–Sc-based alloys (Al–0.12Sc and Al–0.042Sc–0.009Yb, all compositions below are in at.%) and their counterparts with Li-additions (Al–2.9Li–0.11Sc and Al–5.5Li–0.048Sc–0.009Yb) were cast, homogenized at 640 °C, and aged at 325 °C. The following conclusions were reached:

1. For isothermal aging at 325 °C, addition of 2.9 at.% Li to Al–0.12Sc results in a modest increase in peak hardness and a large increase in time to over-aging: from 704 ± 51 MPa over 1–24 h aging, to 806 ± 49 MPa over 0.3–96 h. The increase in microhardness is due to Li, which both provides solid-solution strengthening and creates a larger volume fraction of precipitates at a greater number density and with a smaller mean radius (Table 3). A larger addition of 5.53 at.% Li to the more dilute alloy Al–0.042Sc–0.0088Yb results in a large increase in peak hardness according to the same mechanism: from 376 ± 43 MPa over 0.3–96 h to 688 ± 40 MPa over 0.5–24 h.
2. A second aging treatment at 170 °C of Al–5.53Li–0.048Sc–0.0092Yb, previously peak-aged at 325 °C for 2 h, adds a small hardness increment, from 688 ± 40 to 773 ± 16 MPa. For an Al–Li–Sc–RE-based alloy, which would have high ambient-temperature strength in the doubly-aged state, and still remain coarse-grained and hence creep-resistant, the concentration of Li is restricted to $\sim 5.5 < C_{Li} < 6.3$ at.%.
3. For all alloys peak-aged at 325 °C, all solutes (Li, Sc, Si and Yb) partition strongly to the α' -Al₃(Sc,Li,Yb) precipitates. Yb partitions to the precipitate cores, while Li, Sc and Si are evenly distributed throughout the precipitates. For Al–5.53Li–0.048Sc–0.0092Yb doubly-aged at 325 °C and then at 170 °C, larger metastable δ' -Al₃Li precipitates envelop multiple finer α' -Al₃(Sc,Li,Yb) precipitates formed at 325 °C.
4. The Li and Sc concentrations of α' -Al₃(Sc,Li) precipitates in Al–2.9Li–0.11Sc evolve temporally during aging at 325 °C. The Li concentration decreases from 9.1 ± 0.2 at.% at 8 h to 5.66 ± 0.06 at.% at 1536 h, while the Sc concentration increases from 17.3 ± 0.3 at.% at 8 h to 21.5 ± 0.1 at.% at 1536 h. A lithium addition to Al–Sc reduces energetic barriers to precipitate nucleation, leading to the following observations in Al–2.9Li–0.11Sc compared with Al–0.12Sc aged at 325 °C: (i) a fivefold reduction in the incubation time to a hardness increase; (ii) a fourfold increase in the time to over-aging; (iii) a larger number density of smaller precipitates in the peak-aged state.
5. Throughout the entire aging treatment of Al–2.9Li–0.11Sc at 325 °C, the mean radius of the α' -Al₃(Sc,Li) precipitates increases and the number density decreases. The precipitate volume fraction peaks at $0.557 \pm 0.003\%$ at 8 h, then decreases to $0.451 \pm 0.002\%$ at 1536 h, owing to a decrease in Li concentration in the α' -Al₃(Sc,Li) precipitates from 9.1 ± 0.2 to 5.66 ± 0.06 at.%.

Acknowledgements

This research is supported by the United States Department of Energy (Basic Energy Science) through grant DE-FG02-98ER45721. The LEAP tomography system was

purchased and upgraded with funding from NSF-MRI (DMR-0420532) and ONR-DURIP (N00014-0400798, N00014-0610539, and N00014-0910781) grants. ME Krug would like to thank Drs. C. Booth-Morrison and D. Isheim for helpful discussions.

References

- [1] Knipling KE, Dunand DC, Seidman DN. *Zeitschrift für Metallkunde* 2006;97:246.
- [2] Toporova LS, Eskin DG, Kharakterova ML, Dobatkina TB. *Advanced aluminum alloys containing scandium*. Amsterdam: Gordon & Breach; 1998.
- [3] Drits MY, Ber LB, Bykov YG, Toropova LS, Anastas'eva GK. *Phys Metal Metallogr* 1984;57:118.
- [4] Røyset J, Ryum N. *Int Mater Rev* 2005;50:19.
- [5] Hyland Jr RW. *Metall Mater Trans A* 1992;23:1947.
- [6] Marquis EA, Seidman DN. *Acta Mater* 2001;49:1909.
- [7] Marquis EA, Seidman DN, Dunand DC. *Acta Mater* 2003;51:285.
- [8] Seidman DN, Marquis EA, Dunand DC. *Acta Mater* 2002;50:4021.
- [9] Naumov A. *Russ J Non-Ferrous Metal* 2008;49:14.
- [10] Sawtell RR. *Exploratory alloy development in the system Al-Sc-X*. Ph.D. Thesis, University of California, Berkeley; 1988.
- [11] Sawtell RR, Morris J. *Dispersion strengthened aluminum alloys*. Warrendale: TMS; 1988. p. 409.
- [12] Harada Y, Dunand DC. *Mater Sci Forum* 2007;539–543:1565.
- [13] Harada Y, Dunand DC. *Intermetallics* 2009;17:17.
- [14] van Dalen ME, Dunand DC, Seidman DN. *J Mater Sci* 2006;41:7814.
- [15] Karnesky RA, Seidman DN, Dunand DC. *Mater Sci Forum* 2006;519–521:1035.
- [16] Karnesky RA, van Dalen ME, Dunand DC, Seidman DN. *Scripta Mater* 2006;55:437.
- [17] Krug ME, Werber A, Dunand DC, Seidman DN. *Acta Mater* 2010;58:134.
- [18] Fuller CB, Seidman DN, Dunand DC. *Acta Mater* 2003;51:4803.
- [19] van Dalen ME, Dunand DC, Seidman DN. *Acta Mater* 2005;53:4225.
- [20] Fuller CB, Murray JL, Seidman DN. *Acta Mater* 2005;53:5401.
- [21] Fuller CB, Seidman DN. *Acta Mater* 2005;53:5415.
- [22] Knipling KE, Karnesky RA, Lee CP, Dunand DC, Seidman DN. *Acta Mater* 2010;58:5184.
- [23] Zakharov VV. *Metal Sci Heat Treat* 2003;45:246.
- [24] van Dalen ME, Seidman DN, Dunand DC. *Acta Mater* 2008;56:4369.
- [25] Marquis EA, Riesterer JL, Seidman DN, Larson DJ. *Microsc Microanal* 2006;12:914.
- [26] Marquis EA, Seidman DN. *Surf Interface Anal* 2004;36:559.
- [27] Marquis EA, Seidman DN. *Acta Mater* 2005;53:4259.
- [28] Marquis EA, Seidman DN, Asta M, Woodward C. *Acta Mater* 2006;54:119.
- [29] Marquis EA, Seidman DN, Asta M, Woodward C, Ozolins V. *Phys Rev Lett* 2003;91:036101.
- [30] Marquis EA, Seidman DN, Dunand DC. *Acta Mater* 2003;51:4751.
- [31] Marquis EA, Seidman DN, Dunand DC. In: Zin J, Beaudoin A, Bieler TA, Radhakrishnan B, editors. *Hot deformation of aluminum alloys III*. Warrendale, PA: Springer; 2003. p. 177.
- [32] Miura Y, Horikawa K, Yamada K, Nakayama M. *Aluminum alloys: their physical and mechanical properties*, vol. 2. Atlanta, USA: Georgia Inst. of Technology; 1994. p. 161.
- [33] Joh C, Yamada K. *Mater Trans, JIM* 1999;40:439–42.
- [34] Beresina AL, Kolobnev NI, Chuistov KV, Kotko AV, Molebny OA. *Mater Sci Forum* 2002;396–402:977–82.
- [35] Berezina AL, Volkov VA, Ivanov CV, Kolobnev NI, Chuistov KV. *Fiz Met Metalloved* 1991;2:172.
- [36] Krug ME, Dunand DC, Seidman DN. *Appl Phys Lett* 2008;92.
- [37] Emigh RA. *The aluminum–scandium–lithium–magnesium system as a potential source of superplastically formable alloys*. Ph.D. Thesis, University of California, Berkeley; 1990.
- [38] Emigh RA, Bradley EL, Morris JW. In: Lee EW, Kim NJ, editors. *Light-weight alloys for aerospace applications II*: TMS, Warrendale, PA; 1991. p. 27.
- [39] Radmilovic V, Tolley A, Marquis EA, Rossell MD, Lee Z, Dahmen U. *Scripta Mater* 2008;58:529.
- [40] Monachon C, Krug ME, Dunand DC, Seidman DN. *Acta Mater*; submitted for publications.
- [41] Monachon C, Dunand DC, Seidman DN. *Small* 2010;6:1728.
- [42] Marquis EA, Hyde JM. *Mater Sci Eng: R Rep* 2010;69:37.
- [43] Seidman DN. *Annu Rev Mater Res* 2007;37:127.
- [44] Seidman DN, Stiller K. *MRS Bull* 2009;34:717.
- [45] Seidman DN, Stiller K. *MRS Bull* 2009;34:892.
- [46] Miller MK, Smith GDW. *J Vac Sci Technol* 1981;19:57.
- [47] Hellman OC, Vandenbroucke JA, Rusing J, Isheim D, Seidman DN. *Microsc Microanal* 2000;6:437.
- [48] Miller MK, Kenik EA. *Microsc Microanal* 2004;10:336.
- [49] Murray JL. *J Phase Equilib* 1998;19:380–4.
- [50] Levine E, Rapperport E. *Trans Metall Soc AIME* 1963;227:1204.
- [51] Bevington PR, Robinson DK. *Data reduction and error analysis for the physical sciences*. New York: McGraw-Hill; 2002.
- [52] Jeon SM, Park JK. *Acta Mater* 1996;44:1449.
- [53] Kalogeridis A, Pesicka J, Nembach E. *Acta Mater* 1999;47:1953.
- [54] Messerschmidt U, Bartsch M. *Mater Sci Eng A* 1993;164:332.
- [55] Miura Y, Matsui A, Furukawa M, Nemoto M. In: Baker C, Gregson PJ, Harris SJ, Peel CJ, editors. *Aluminium–lithium alloys III*. London: Inst. of Metals; 1986. p. 427.
- [56] Nembach E. *Prog Mater Sci* 2000;45:275.
- [57] Noble B, Harris S, Dinsdale K. *Metal Sci* 1982;16:425.
- [58] Schlesier C, Nembach E. *Acta Metall Mater* 1995;43:3983.
- [59] Noble B, Bray SE. *Acta Mater* 1998;46:6163–71.
- [60] Tsao C-S, Chen C-Y, Kuo T-Y, Lin T-L, Yu M-S. *Mater Sci Eng A* 2003;363:228.
- [61] Hono K, Babu SS, Hiraga K, Okano R, Sakurai T. *Acta Metall Mater* 1992:40.
- [62] Noble B, Thompson GE. *Metal Sci* 1971;5:114–20.
- [63] Fujikawa S, Izeki Y, Hirano K. *Scr Metall* 1986;20:1275.
- [64] Ceresara S, Giarda A, Sanchez A. *Philos Mag* 1977;35:97.
- [65] Nozato R, Izawa H, Tsubakino H. *J Jpn Inst Metal* 1980;44:1203.
- [66] Kelly A, Nicholson RB. *Prog Mater Sci* 1963;10:151.
- [67] Hillel AJ. *Acta Metall* 1970;18:253.
- [68] Jo H-H, Fujikawa S-I. *Mater Sci Eng A* 1993;171:151.
- [69] Ocko M, Babic E, Krsmik R, Girt E, Leontic B. *J Phys F-Metal Phys* 1976;6:703.
- [70] Rossiter PL. *The electrical resistivity of metals and alloys*. Cambridge: Cambridge University Press; 1987.
- [71] Fridlyander I, Rokhlin L, Dobatkina T, Nikitina N. *Metal Sci Heat Treat* 1993;35:567–71.
- [72] Raghavan V. *J Phys Equilib Diff* 2009;30:189.
- [73] Beeri O, Dunand DC, Seidman DN. *Mater Sci Eng A* 2010;527:3501.
- [74] Du G, Deng J, Wang Y, Yan D, Rong L. *Scripta Mater* 2009;61:532.
- [75] van Dalen ME. *Microstructure and creep properties of Al–Sc alloys micro-alloyed with lanthanides (Yb or Gd) and transition metals (Ti or Zr)*. Ph.D. Thesis, Northwestern University, Evanston; 2007.
- [76] Sutton AP, Balluffi RW. *Interfaces in crystalline materials*. Oxford, New York: Clarendon Press, Oxford University Press; 1995.
- [77] Isheim D, Gagliano MS, Fine ME, Seidman DN. *Acta Mater* 2006;54:841.
- [78] Dregia SA, Wynblatt P. *Acta Metall Mater* 1991;39:771.
- [79] Defay R, Prigogine I, Bellemans A. *Surface tension and adsorption*. New York: Wiley; 1966.
- [80] Shashkov DA, Muller DA, Seidman DN. *Acta Mater* 1999;47:3953.
- [81] Shashkov DA, Seidman DN. *Phys Rev Lett* 1995;75:268.
- [82] Dregia SA, Wynblatt P. *Acta Metall Mater* 1991;39:771.
- [83] Defay R, Prigogine I, Bellemans A. *Surface tension and adsorption*. Wiley; 1966.
- [84] Hellman OC, Seidman DN. *Mater Sci Eng A* 2002;327:24.
- [85] Asta M, Ozolins V, Woodward C. *JOM* 2001;53:16.
- [86] Iwamura S, Miura Y. *Acta Mater* 2004;52:591.

- [87] Novotny GM, Ardell AJ. *Mater Sci Eng A* 2001;318:144.
- [88] Robson JD, Jones MJ, Prangnell PB. *Acta Mater* 2003;51:1453.
- [89] Røyset J, Ryum N. *Mater Sci Eng A* 2005;396:409.
- [90] Watanabe C, Kondo T, Monzen R. *Metall Mater Trans A* 2004;35:3003.
- [91] Kuehmann CJ, Voorhees PW. *Metall Mater Trans A* 1996;27:937.
- [92] Mao Z, Chen W, Seidman DN, Wolverton C. *Acta Mater*; Submitted for publications.
- [93] Wagner R, Kampmann R. Homogeneous second phase precipitation. In: Haasen P, Cahn RW, Haasen P, Kramer EJ, editors. *Phase transformations in materials*, vol. 4. New York: John Wiley; 1991. p. 213.
- [94] Martin G. *Solid state phase transformation in metals and alloys*. Orsay: Les Editions de Physique; 1978.
- [95] Pearson WB. *A handbook of lattice spacings and structures of metals and alloys*. London: Pergamon Press; 1967.
- [96] Yoshi-yama T, Hasebe K, Mannami M-h. *J Phys Soc Jpn* 1968;25:908.
- [97] Hallstedt B, Kim O. *Int J Mater Res* 2007;98:961.